buildings

MDPI

Article

Impact Resistance of Rubberized Alkali-Activated Concrete Incorporating Recycled Aggregate and Recycled Steel Fiber

Weixian Che [1], Lei Li [2], Zhongmin Chen [2], Donghua Liang [3] and Yongchang Guo [3,*]

[1] Grid Planning and Research Center, Guangdong Power Grid Co., Ltd., China Southern Power Grid Co., Ltd., Guangzhou 510006, China; 15915791023@139.com
[2] Maoming Power Supply Bureau, Guangdong Power Grid Co., Ltd., China Southern Power Grid Co., Ltd., Maoming 525000, China; 13580020513@139.com (L.L.); 13727802693@139.com (Z.C.)
[3] School of Civil and Transportation Engineering, Guangdong University of Technology, Guangzhou 510006, China; a623633772@126.com
* Correspondence: guoyc@gdut.edu.cn; Tel.: +86-203-9322-538

Abstract: Alkali-activated concrete (AAC) features excellent mechanical properties and sustainability. The incorporation of crumb rubber (CR), recycled concrete aggregates (RCAs), and recycled steel fibers (RSFs) can further enhance environmental sustainability. This paper mainly investigated the dynamic behaviors of a novel rubberized AAC incorporating RCAs and RSFs (RuAAC) through Split-Hopkinson Pressure Bar (SHPB) tests. The variables included three types of RSF content (1%, 2% and 3%), five types of rubber content (0%, 5%, 20%, 35% and 50%) and five impact pressures (0.5 MPa, 0.6 MPa, 0.7 MPa, 0.8 MPa and 0.9 MPa). Dynamic stress–strain curves, dynamic strength, the dynamic increase factor (DIF), impact toughness and the synergistic effects of RSF and CR were discussed. The results show that increasing RSF and CR contents could improve the impact resistance of RuAAC under impact loading. The RuAAC exhibited significant strain rate sensitivity, and the sensitivity increased with larger contents of RSF and CR. The increase in strain rate sensitivity was more pronounced with higher CR contents, which was reflected in larger dynamic increase factor (DIF) values. Under high impact pressure, the impact toughness was obviously enhanced with higher RSF contents, while the contribution of increased CR content to impact toughness was not apparent, which may be attributed to the fact that this study only calculated the integral under the dynamic stress–strain curve before the peak stress to determine impact toughness, neglecting the potential contribution of CR particles after the peak point. The obvious strain sensitivity exhibited by the RuAAC in the SHPB tests indicated superior impact performance, making it particularly suitable for architectural structures prone to seismic or explosive impacts.

Keywords: rubberized alkali-activated concrete; recycled steel fiber; recycled aggregate; impact loading; SHPB test

Citation: Che, W.; Li, L.; Chen, Z.; Liang, D.; Guo, Y. Impact Resistance of Rubberized Alkali-Activated Concrete Incorporating Recycled Aggregate and Recycled Steel Fiber. *Buildings* **2024**, *14*, 322. https://doi.org/10.3390/buildings14020322

Academic Editors: José Marcos Ortega and Fernando G. Branco

Received: 29 December 2023
Revised: 14 January 2024
Accepted: 18 January 2024
Published: 24 January 2024

1. Introduction

Alkali-activated concrete (AAC) is a three-dimensional inorganic binder material formed by precursor materials under the action of alkali activation [1–3]. Precursors often consist of industrial solid waste rich in silica and alumina, such as fly ash (FA), ground granulated blast-furnace slag (GGBS), steel slag (SS), coal ash (CA), and metakaolin (MK), rather than the cement used in traditional concrete [1,4,5]. Cement, a construction material that is widely used globally, emits a substantial amount of carbon dioxide during its production (approximately 1 ton of CO_2 per ton of cement) [6], contributing to the greenhouse effect and hindering sustainable development in the construction industry [7]. To mitigate global greenhouse gas emissions, novel materials and structures are necessary for carbon reduction [8–10]. AAC, capable of achieving similar or even superior mechanical properties to conventional concrete without cement clinker, has become a prominent topic in the field of concrete materials research [11–13]. However, continuous growth in the

demand for natural aggregates (NAs) in concrete places significant pressure on resources and the environment. Utilizing construction waste, discarded tires, and other solid wastes to produce recycled concrete aggregates (RCAs) as substitutes for NAs can alleviate the demand for NAs in construction and reduce environmental pollution [14–17].

In recent years, extensive research has been conducted on the reaction mechanism and products of AAC [18–20]. Under conditions of strong alkali solution stimulation, chemical bonds in the precursor materials break, leading to the formation of two main reaction products with cross-linked and disordered structures, N-A-S-H and C-A-S-H gels [20,21]. With the continuous generation and precipitation of the main reaction products, AAC ultimately achieves mechanical properties comparable to traditional concrete [22,23]. Reports in the literature indicated that the compressive strength of AAC was mainly influenced by the ratio of precursors, alkali activator content (alkali activator/precursor), alkali activator concentration, and so on [24–26]. Lian, et al. [23] developed AACs with average compressive strengths exceeding 30 MPa (FA/GGBS = 9.0) and 60 MPa (FA/GGBS = 1.0) by adjusting the FA/GGBS ratio and water-to-binder ratio. It was noted that an excessively high fly ash content or inappropriate alkali activator dosage was detrimental to the compressive strength development of AAC, consistent with some literature reviews [24–26].

Due to its rapid setting characteristics and excellent mechanical properties, AAC also has potential for applications in military construction. Combining RCAs, CRs, RSFs and other recycled materials can further enhance the environmental friendliness of AAC. Currently, research has only been conducted on AAC using a single type or two types of recycled raw materials [27]. RCAs derived from construction waste should undergo quality control, including proper screening and crushing, as well as the removal of impurities and adhering mortar [28]. The presence of residual mortar, cracks and high porosity on RCA surfaces typically leads to a decline in the mechanical properties of concrete. For instance, shear strength tests conducted by Imjai et al. [29] indicated a consistent decrease in shear strength when an RCA replaces an NA. Regarding structural performance, Imjai et al. [30] observed that in fiber-reinforced and polymer-reinforced slabs with comparable reinforcement ratios, the maximum capacity of recycled aggregate concrete (RAC) slabs consistently fell below that of their counterparts using natural aggregate concrete. Furthermore, Kefyalew et al. [31] noted a modest reduction in flexural capacity, with a 7% decrease in slabs incorporating 100% RCA. However, the impact on the slabs' energy absorption was more substantial, showing a more pronounced reduction of up to 22%. Overall, RAC exhibited lower mechanical properties depending on the level of replacement with an RCA. However, experimental results still showed inconsistencies, especially when employing a significant amount of RCA, such as complete substitution (100% replacement of NA). Therefore, further research in this area is deemed necessary.

When a large amount of CR was used in AAC, regardless of the precursor, alkali solution and curing conditions, the compressive strength tended to decrease [32,33]. The decrease in compressive strength was usually attributed to weaker interfacial transition zones (ITZs), the lower elastic modulus of rubber particles, uneven mixing caused by rubber and increased bubbles, among other factors [34,35]. Meanwhile, fibers are commonly employed to mitigate brittle failure due to AAC's more pronounced brittleness compared to ordinary concrete [36,37]. RSFs derived from discarded tires exhibited mechanical properties similar to industrial steel fibers (SFs), making them a suitable replacement for SFs [38,39]. Peng et al. [40] demonstrated that RSFs significantly enhanced the strength and toughness of ultra-high-performance concrete (UHPC), contributing to preventing immediate fiber pull-off. Test results from Zhuo, et al. [39] indicated that the incorporation of CR would decrease the mechanical properties of UHPC, while RSFs contributed to improve ductility and compressive strength properties due to their crack-bridging effect. Chen, et al. [4] developed high-performance geopolymer concrete (R-HPGC) with RSFs and CR, indicating that the compressive performance of the R-HPGC was influenced by the mechanical properties and interactions among the combined aggregates, matrix and RSFs. Furthermore, the synergistic effect of RSFs and CR was demonstrated by

Liu et al. [41]. However, despite the appeal of combining RCAs, RSFs and CR in rubberized AAC (RuAAC), there is still limited research on the impact performance of such materials.

This paper proposed a novel RuAAC that combines CR, RCAs and RSFs. The influence of different RSF and CR contents on the static and dynamic compressive mechanical properties of the RuAAC were studied using axial compression tests and SHPB tests. The discussion below includes the failure mode, stress–strain curves, dynamic compressive strength, DIF and toughness of the RuAAC. Furthermore, the toughening mechanisms of RSFs and CR in the RuAAC ae discussed.

2. Experimental Program

2.1. Materials and Mix Proportion

The raw materials used in this paper are shown in the macroscopic morphology images in Figure 1 and are mainly divided into precursors, aggregates, alkali activators, fibers and a retarder. The precursors included FA (Class F) and GGBS (S95), with their particle size distribution and microscopic morphology under scanning electron microscopy (SEM) shown in Figure 2. Additionally, X-ray diffraction (XRD) patterns of the precursors are shown in Figure 3. And the chemical compositions of the FA and GGBS were determined using an X-ray fluorescence (XRF) test, the results of which are shown in Table 1. The alkaline activator was a mixture of sodium hydroxide (SH) and sodium silicate (SS). The SH was sourced from Xilong Scientific Co., Ltd. (Shenzhen, China) and was a white, uniformly granular solid with a purity of ≥96.0%. (NaOH). Detailed parameters of the SS are listed in Table 2. Note that the alkali-activated solution was prepared by mixing a pre-prepared SH solution with SS. The molarity of the SH solution was 10 mol/L.

Figure 1. Raw materials of RuAAC.

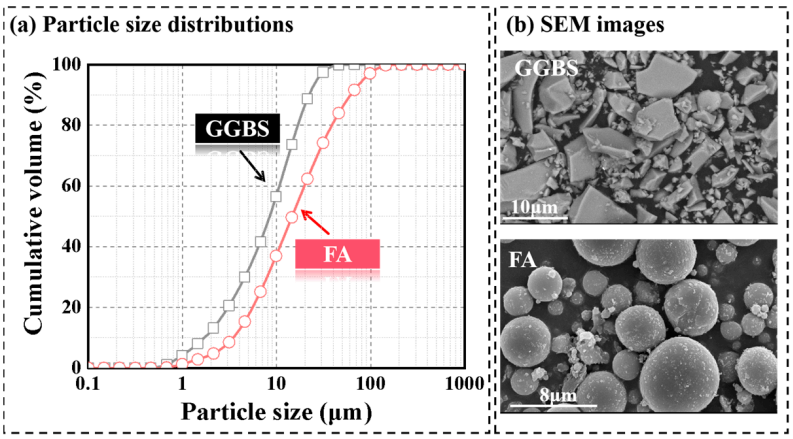

Figure 2. Raw materials: (**a**) particle size distributions; (**b**) SEM images.

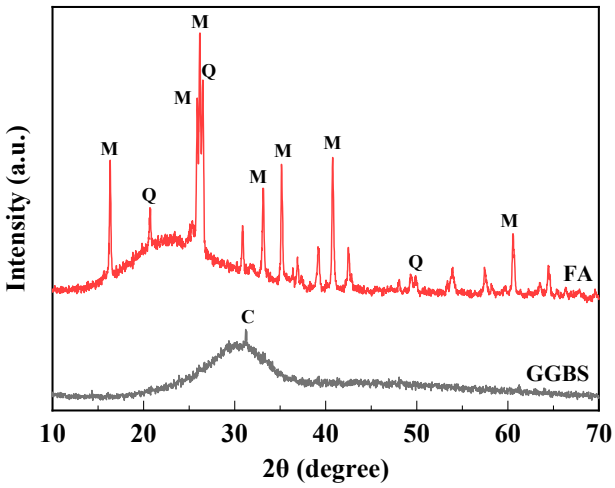

Figure 3. XRD patterns for FA and GGBS (M = mullite; Q = quartz; C = $Ca_3Al_2Si_2$).

Table 1. Chemical compositions of GGBS and FA (unit: wt%).

	CaO	SiO_2	Al_2O_3	SO_3	Fe_2O_3	MgO	TiO_2	Others	LOI (%)
GGBS	34.00	34.50	17.70	1.64	1.03	6.01	/	5.12	0.84
FA	4.01	53.97	31.15	2.20	4.16	1.01	1.13	2.37	4.60

Note: LOI denotes loss on ignition.

Table 2. Detailed parameters of SS solution.

	Molarity	Density (g/cm^3)	SiO_2 (%)	Na_2O (%)	H_2O (%)
SS	2.25	1.5	29.99	13.75	56.26

The aggregates consisted of recycled coarse aggregates (RCAs), river sand (RS) and crumb rubber (CR). According to GB/T 14685-2022 [42], the RS was medium sand with a fineness modulus of 2.34 and an apparent density of 2650 kg/m^3. To eliminate the influence of particle size on the performance of the RuAAC, the particle size distribution of the CR used in this paper was similar to that of the RS, with a particle size of 0.3–1.1 mm, as shown in Figure 4. The RCA was a continuous graded recycled concrete aggregate with a particle size of 5–10 mm, and its basic performance indicators are shown in Table 3. Furthermore, in this study, recycled steel fibers (RSFs) were adopted instead of the commonly used copper-plated steel fibers. RSFs were recovered from steel wires in shredded waste tires. In order to characterize the length of RSFs, previous studies have employed multiple random samplings to measure and count the lengths of 460 RSFs and fitted them using a log-normal distribution function. The frequency distribution of RSF lengths can be found in Ref. [4]. In addition, barium chloride ($BaCl_2$) was used as a retarding agent to prevent the rapid setting of the RuAAC.

Table 4 presents the mix proportions for the seven groups of RuAAC. In this paper, the seven groups of RuAAC were prepared and named SFa-Rb, where a and b represent the volume content of RSFs (1–3%) and the rubber content (0–50%), respectively. The fiber content of 1–3% adopted in this study was generally used in previous studies [4,17,40]. The rubber content was limited to below 50% because an excessively high rubber content will lead to poor workability based on trial-and-error experiments and existing studies [4,43]. To satisfy the workability and setting time requirements of RuAAC, the water-to-binder ratio was fixed at 0.35. It is worth noting that the volume of water included the water in the solutions of SH and SS. The binder-to-aggregate ratio was fixed at 3.5. Additionally, the weight of the added $BaCl_2$ was controlled at 1% of the binder material.

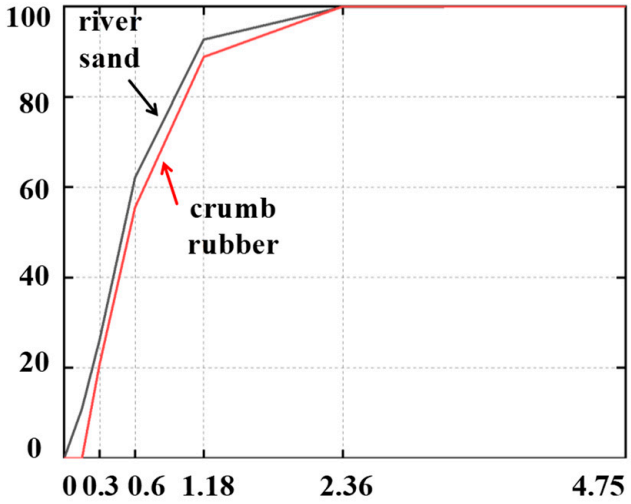

Figure 4. Grading distribution of river sand and crumb rubber.

Table 3. Basic properties of recycled concrete aggregate.

Size (mm)	Apparent Density (kg/m^3)	Bulk Density (kg/m^3)	Water Absorption (%)
5–10	2658	1301	4.71

Table 4. Mix proportions (unit: kg/m^3).

Mix IDs	FA [1]	GGBS [2]	RCA [3]	RS [4]	CR [5]	SS [6]	SH [7]	Water	$BaCl_2$	RSF [8]
RSF1-R0	390.0	260.0	1083.3	541.7	0	220.2	20.2	103.6	6.5	78.5
RSF2-R0	390.0	260.0	1083.3	541.7	0	220.2	20.2	103.6	6.5	157.0
RSF3-R0	390.0	260.0	1083.3	541.7	0	220.2	20.2	103.6	6.5	235.5
RSF2-R5	390.0	260.0	1083.3	514.6	12.2	220.2	20.2	103.6	6.5	157.0
RSF2-R20	390.0	260.0	1083.3	433.7	48.5	220.2	20.2	103.6	6.5	157.0
RSF2-R35	390.0	260.0	1083.3	352.1	85.0	220.2	20.2	103.6	6.5	157.0
RSF2-R50	390.0	260.0	1083.3	270.9	121.4	220.2	20.2	103.6	6.5	157.0

[1] fly ash; [2] ground granulated blast-furnace slag; [3] recycled concrete aggregates; [4] river sand; [5] crumb rubber; [6] sodium silicate; [7] sodium hydroxide; [8] recycled steel fibers.

2.2. Specimens and Preparation

The preparation process of RuAAC is shown in Figure 5. The preparation of RuAAC in this study used a forced mixer with a mixing speed of 48 r/min. Before mixing, the mixer was wetted with water. To ensure uniform mixing of binder materials and aggregates, FA and GGBS were first added and mixed for 3 min. RCAs, RS and CR were then added and mixed for another 3 min. The alkali-activated solutions were added and stirred for 3 min to form a homogeneous alkali-activated mortar. Finally, fibers were slowly added and stirred for 3 min to ensure even dispersion. The freshly mixed RuAAC was poured into molds, placed on a vibrating table, and compacted using a tamping rod simultaneously with vibration. After compaction, the surfaces of the specimens were smoothed. Finally, a thin plastic film was placed over the specimens to avoid water evaporation. All the specimens were demolded and subsequently underwent preservation in room for 24 h. The specimens were cured by sprinkling water on them for 27 d until formal tests were conducted.

The test specimens for the axial compression test in this study were cylindrical specimens with a diameter of 100 mm and a height of 200 mm, while the specimens for the SHPB test were disk-shaped specimens with a diameter of 100 mm and a height of 50 mm.

Figure 5. Mixing process.

3. Experimental Setup and Procedure

3.1. Axial Compression Test

Test equipment for a static axial compression test is shown in Figure 6. As per ASTM C469 [44], a static axial compression test was conducted on cylindrical specimens using a testing machine with a maximum capacity of 4000 kN. Initially, gypsum was used to level the top and bottom of each specimen to avoid loading eccentricity. Four 50 mm strain gauges were attached to each specimen's surface to obtain axial strains and hoop strains. Meanwhile, two symmetrically placed linear variable differential transformers (LVDTs) with a gauge length of 80 mm were adopted to obtain axial deformation at mid-height of the specimens. In order to obtain complete stress–strain curves, a displacement loading mode with a rate of 0.12 mm/min was applied. Displacement, axial strain, hoop strain and force were acquired simultaneously using a TDS-530 high-speed static strain gauge with a data acquisition frequency of 1 Hz.

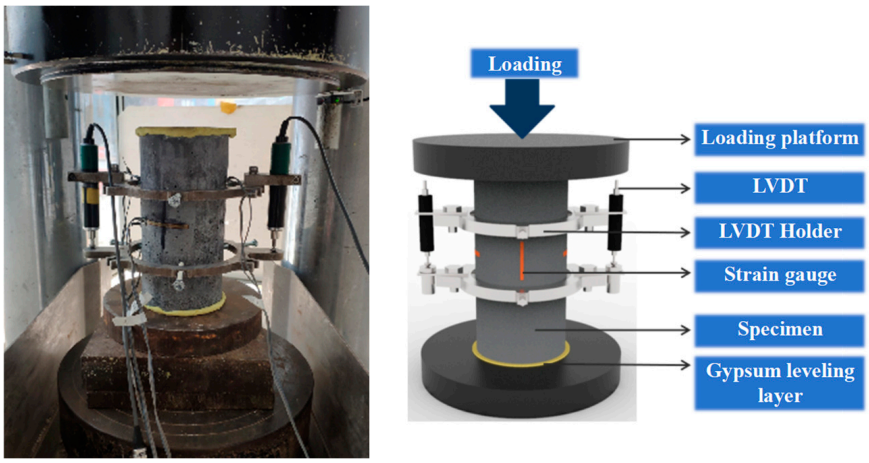

(**a**) (**b**)

Figure 6. Test equipment for static axial compression test: (**a**) test setup; (**b**) schematic diagram.

3.2. Split-Hopkinson Pressure Bar Test

This paper employed the Split-Hopkinson Pressure Bar (SHPB) test method, and the experimental setup and schematic diagram are illustrated in Figure 7, with the critical pa-

rameters of the test equipment for the SHPB test shown in Table 5. The SHPB experimental apparatus includes a striker and incident, transmission and absorption bars, as specifically shown in Figure 7. To avoid the influence of surface roughness at the contact interface on the RuAAC's impact performance, the contact surfaces of the specimens were polished before the experiment to ensure that the surface roughness was less than 0.02 mm [45,46]. To eliminate the high-frequency influence of stress waves and prolong the rising time of the incident wave, a brass pulse shaper with a diameter of 20 mm and a thickness of 2 mm was used [45,47,48]. Strain gauges were attached to the incident and transmission bars to measure dynamic strains, which were collected at a frequency of 1 MHz using a dynamic strain acquisition instrument. The dynamic stress, dynamic strain and strain rate of specimens can be calculated using the following equations:

$$\sigma(t) = \frac{A_b E_b}{2A_0}[\varepsilon_i(t) + \varepsilon_r(t) + \varepsilon_t(t)] \quad (1)$$

$$\varepsilon(t) = \frac{C_b}{l_0}\int [\varepsilon_i(t) - \varepsilon_r(t) - \varepsilon_t(t)]dt \quad (2)$$

$$\dot{\varepsilon}(t) = \frac{-2C_b}{l_0}\varepsilon_r(t) \quad (3)$$

where $\sigma(t)$ and $\varepsilon(t)$ are the dynamic stress and strain of the specimens, respectively. A_b, E_b and C_b are the cross-sectional area, elastic modulus and elastic wave velocity of the bars. A_0 and l_0 are the cross-sectional area and height of the specimen, respectively.

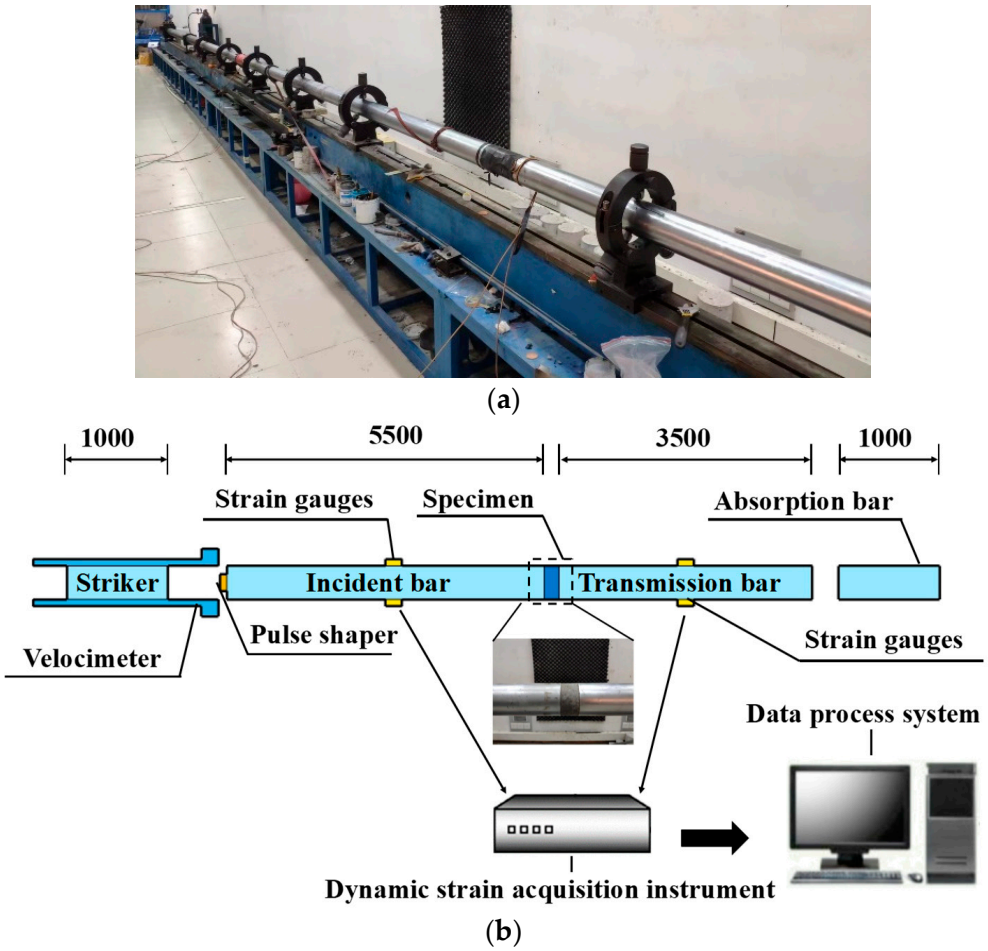

Figure 7. Test equipment for SHPB test: (**a**) test setup; (**b**) schematic diagram.

Table 5. Critical parameters of the test equipment for the SHPB test.

Parameters	Values
Young's modulus	206 GPa
Density	7.71 × 103 kg/m^3
Diameter	100 mm
Elastic wave velocity	5169 m/s
The length of striker	1000 mm
The length of incident bar	5500 mm
The length of transmission bar	3500 mm

4. Results and Discussions

4.1. Static Compressive Behaviors

4.1.1. Failure Mode

The failure modes of the RuAAC groups during the static axial compression test are depicted in Figure 8. While exhibiting slight variations among different RuAAC groups, all specimens maintained structural integrity and displayed a diagonal shear failure mode. The incorporation of RSFs and CR into the RuAAC matrix enabled a ductile failure mode. As the load increased, microcracks initiated and propagated in the matrix, activating the bridging effect of the fibers and providing lateral confinement to the specimen during crack propagation. Therefore, cracks along the loading direction were controlled, delaying the failure of the specimens.

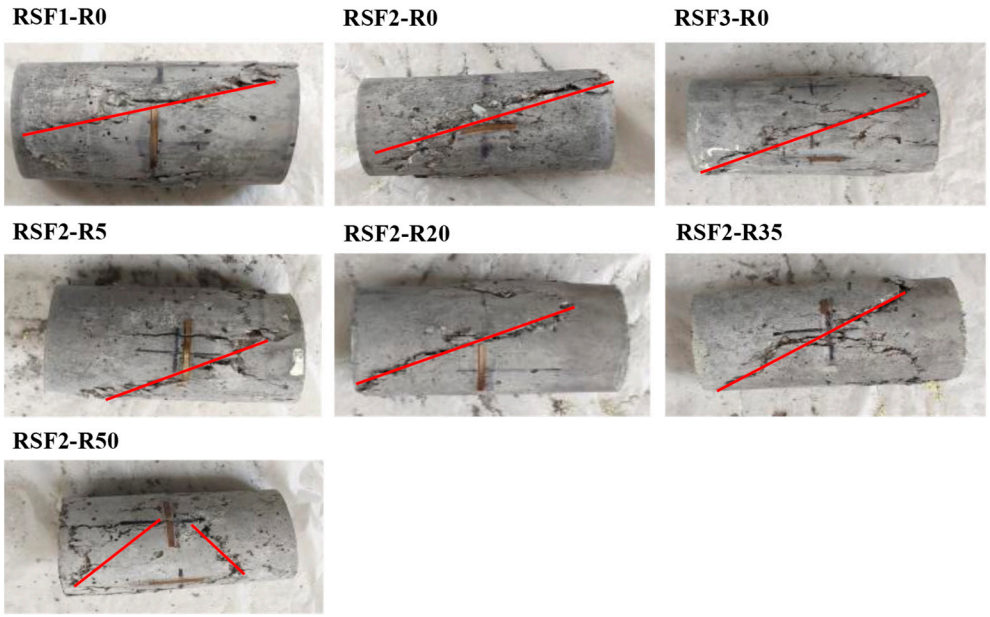

Figure 8. Failure modes of RuAAC for a static compression test.

With increases in RSF and CR contents, the main crack angle of the specimens increased, leading to diagonal shear failure accompanied by multiple diagonal cracks, which was consistent with the test results from Chen, et al. [4]. In particular, when the CR content increased to 50%, the surfaces of the specimens were filled with diagonal cracks, indicating the enhanced deformability and ductile failure of the RuAAC. The augmented ductility could be interpreted via reduced flowability, increasing voids with CR incorporation, as well as poor bonding between the matrix and CR [45]. Additionally, as shown in Figure 8, cracks traversed the entirety of the specimens, with some protrusions in the middle but no spalling. This may be attributed to the effective bridging effect of the RSFs, which suppressed the number and width of cracks, preserving the integrity of the specimens.

4.1.2. Stress–Strain Curves

Figure 9 shows representative stress–strain curves for different RSF and CR contents. From Figure 9a, it can be observed that the peak stress of the concrete increased as the RSF content increased. The slope of the ascending branches of the curves show no clear pattern of change, while the descending branches become more moderate, indicating that RSFs could improve both the strength and ductility of RuAAC. This may be related to the inhibition effect of RSFs on crack propagation. Due to the bridging effect of RSFs, the lateral deformation of the RuAAC was constrained, leading to delayed failure and increased peak stress. The toughening effect of RSFs has been observed in previous studies, consistent with the results of this research [4]. It is worth noting that the toughening effect may be slightly lower than that of SFs due to the varying lengths of RSFs, as demonstrated in other studies [4,39].

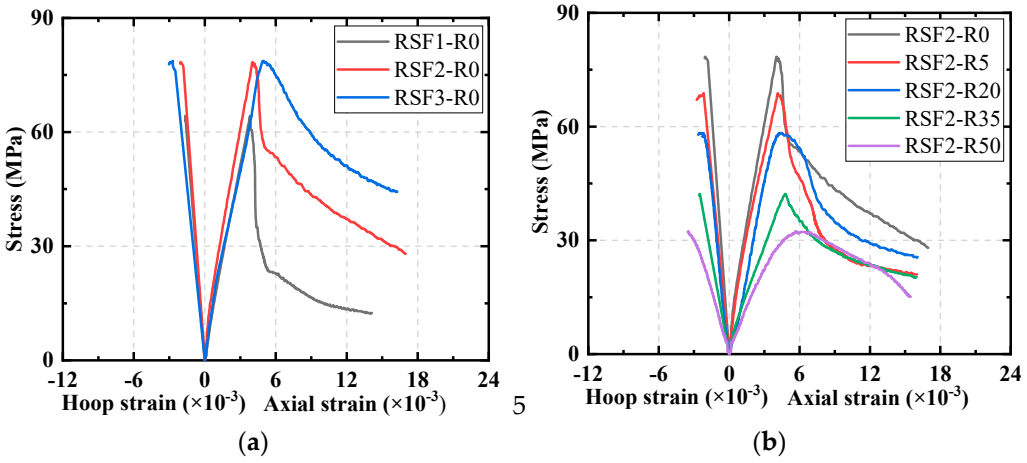

Figure 9. Representative stress–strain curves of RuAAC under axial compression: (**a**) RSF content; (**b**) rubber content.

However, no clear pattern in the influence of the RSF content on the elastic modulus can be found. The elastic modulus was likely primarily influenced by the CR content, as the addition of rubber made the concrete more prone to deformation, as shown in Ref. [39]. As seen in Figure 9b, with an increase in CR content, both the ascending and descending branches of the curves become more moderate while the peak stress obviously declines, showing that CR reduced the compressive strength of the RuAAC but, to some extent, improved its deformability. This can be attributed to the increase in bubbles when CR was introduced and the discontinuity between the matrix and the CR, as well as the low strength and elastic modulus of the CR itself.

4.1.3. Compressive Strength and Elastic Modulus

The results of the static axial compression test are presented in Table 6. Figure 10 shows the effect of different RSF and rubber contents on the static axial compressive strength and elastic modulus of the RuAAC. It could be seen that among all mix proportions, RSF3-R0 reached the highest strength (81.2 MPa). The axial compressive strength of the RuAAC continuously increased with the increase in the RSF content but decreased continuously with the increase in the CR content. As mentioned before, the main reason for this may be that CR has much lower mechanical properties than RS and a poorer rubber–matrix bonding interface. Moreover, the addition of rubber increased the internal pores in the concrete, weakening its compressive strength. The bridging effect of RSFs within the matrix constrained the lateral deformation of the concrete, improving its bearing capacity and ductility. This indicated that the bridging effect of RSFs could compensate for the negative impact of CR on compressive performance to some extent.

Table 6. Results of static compression test.

Mix IDs	Compressive Strength /MPa	Elastic Modulus /GPa
RSF1-R0	66.3 (2.0)	19.2 (0.6)
RSF2-R0	79.6 (1.7)	23.4 (1.7)
RSF3-R0	81.2 (2.1)	21.0 (3.1)
RSF2-R5	70.3 (1.7)	22.6 (5.1)
RSF2-R20	56.7 (1.5)	13.7 (0.8)
RSF2-R35	43.3 (1.2)	11.6 (1.0)
RSF2-R50	30.7 (1.8)	8.0 (0.1)

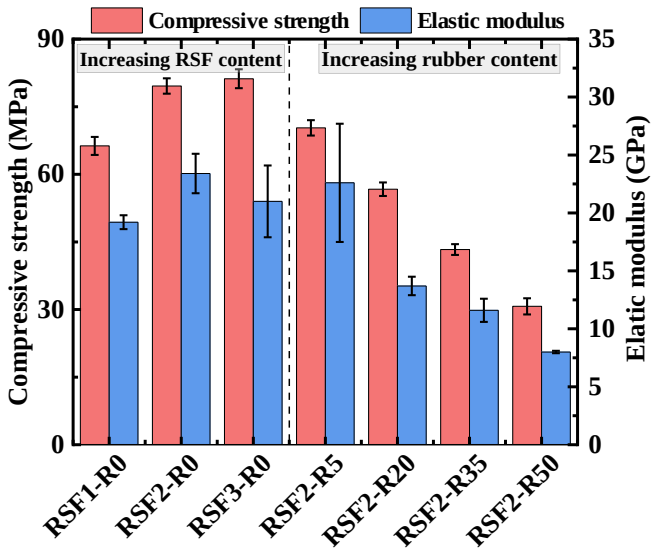

Figure 10. Influence of recycled steel fiber content and rubber content on static compressive strength and elastic modulus.

For the elastic modulus, the increase in RSF content showed no clear pattern of influence, while increasing the CR content ha a noticeable negative impact; in particular, RSF2-R50 reached an elastic modulus of only 8.0 GPa. It was worth noting that the elastic modulus of the RuAAC was significantly lower than that of ordinary Portland concrete (OPC) with the same strength, consistent with existing research results [1,3]. Current prediction models for OPC tend to overestimate the elastic modulus of AAC. It should be noted that the general relationship between the elastic modulus and compressive strength of AAC was still unclear due to limited available data and the variability of the components in AAC.

4.2. Dynamic Compressive Behaviors

4.2.1. Failure Mode

Figure 11 presents the failure modes of the RuAAC at various impact pressures. From Figure 11, it can be observed that the damage to the RuAAC samples with different RSF and rubber contents became more severe with increasing impact pressure. The RuAAC only exhibited a few microcracks, staying relatively intact under low impact pressure, while the RuAAC was completely destroyed and presented a powder-like or fine-chunk state under high impact pressure. Additionally, it can be seen from Figure 11 that the integrity of the RuAAC at the same impact pressure was greater with an increasing RSF content, indicating that RSFs can enhance impact resistance. Similarly, the integrity of the RuAAC specimens also improved to some extent when the rubber content increased. In short, when subjected to impact loading under similar impact pressures, the impact performance of RSF2-R5 was superior to RSF2-R50, with greater integrity. The higher the bridging effect provided by

RSFs, the greater the integrity of the RuAAC. With a greater RSF content, the RuAAC had higher strength and maintained greater integrity. It was worth noting that the extent of RuAAC damage may also be related to the size of the RSFs, since these types of fibers are irregular in length and shape, which may result in different toughening effects on concrete. Additionally, adding CR particles to the RuAAC helped improve its crack resistance ability. When cracks began to propagate toward the center of the specimens, CR played a role in inhibiting crack expansion. The slowing down of the crack propagation rate can be interpreted as the energy dissipation of CR under impact loading. The mechanism allowed the CR to effectively absorb and mitigate the effect of sudden impacts.

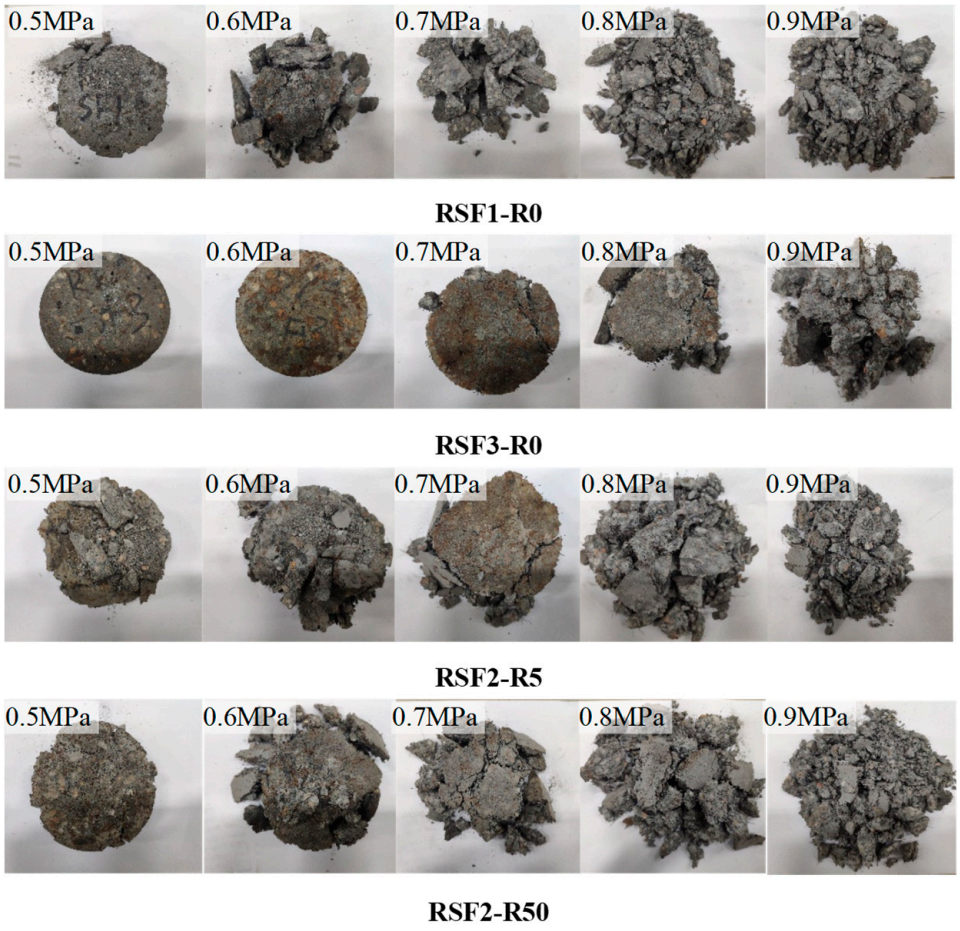

Figure 11. Failure modes.

4.2.2. Dynamic Stress–Strain Curves

Figure 12 illustrates the dynamic stress–strain curves of RuAAC samples with varying contents of RSF and CR under different impact pressures. From Figure 12, it can be observed that the dynamic stress–strain curves of the RuAAC can be divided into ascending and descending branches. First, the curves gradually rose, starting to descend after reaching peak stress. With increasing RSF and CR contents, the descent of the curves became more gradual. At different impact pressures, there was no clear pattern in the rising segments of the curves, but the peak stress was significantly increased, indicating a noticeable strain rate effect in the RuAAC. When the RSF content increased, the peak stress significantly increased, with the slope of the rising segments of the curves slightly increasing, while the falling segments became more gradual. On the other hand, when the rubber content increased, the peak stress decreased, with the slope of the rising segments of the curves slightly decreasing, while the falling segment remained relatively smooth. This indicates that both RSFs and rubber particles delayed the development of cracks and the ultimate failure, demonstrating a significant synergistic toughening effect. Although the SHPB test

results for RuAAC are relatively limited, these observations are generally consistent with the strain rate effect observed in previous studies on rubberized AAC [27,49,50].

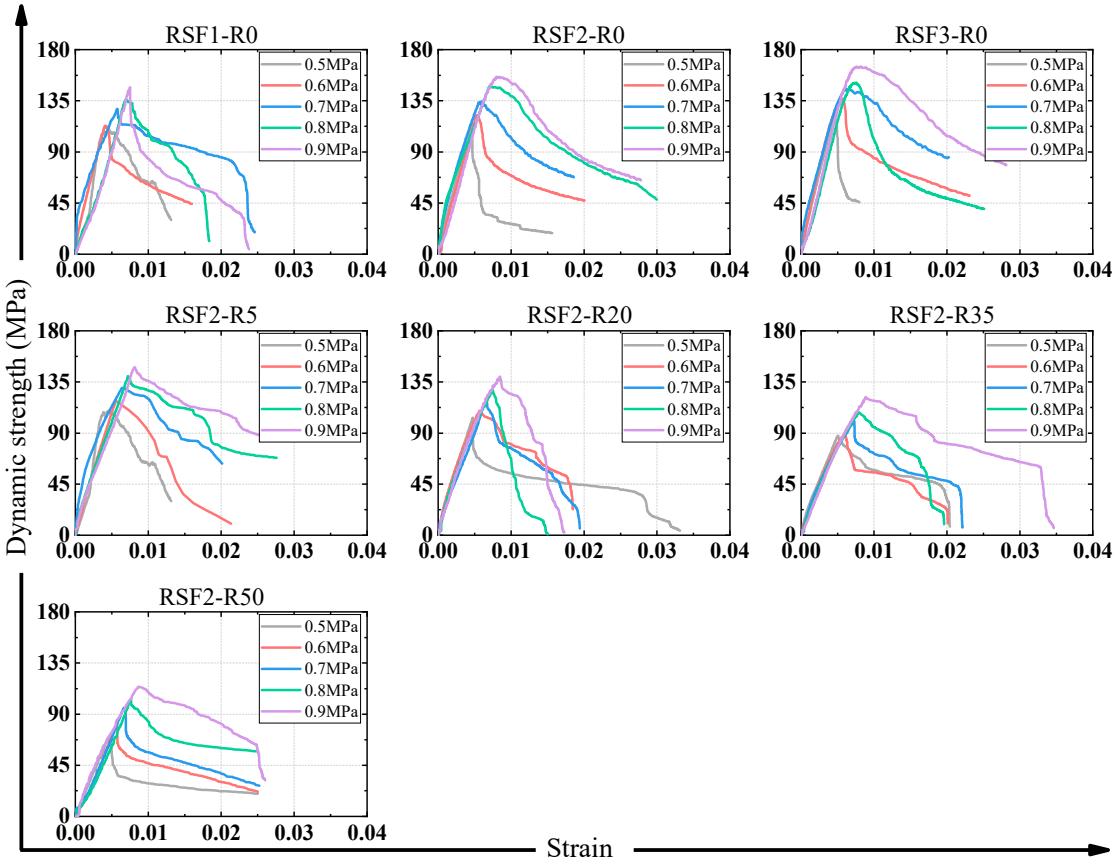

Figure 12. Representative stress–strain curves of RuAAC under different impact pressures.

4.2.3. Dynamic Compressive Strength and DIF

Table 7 summarizes the dynamic compressive strength and dynamic increase factor (DIF) of the RuAAC at different impact pressures. Figure 13 presents the influence of different levels of impact pressure on the dynamic compressive strength of the RuAAC, and Figure 14 illustrates the crack propagation patterns of the RuAAC specimens under different impact pressures. From Figure 13, it can be seen that RuAAC showed obvious sensitivity to impact pressure, with the dynamic compressive strength increasing with an increase in impact pressure. A generally linear relationship between impact pressure and dynamic compressive strength can be observed. For example, the dynamic compressive strength of RSF3-R0 at impact pressures of 0.5 MPa, 0.6 MPa, 0.7 MPa, 0.8 MPa and 0.9 MPa increased to 126.2 MPa by 55.4%, 137.4 MPa by 69.2%, 145.8 MPa by 79.6%, 151.0 MPa by 86.0%, and 165.2 MPa by 103.4%, respectively, attributed to changes in crack propagation paths under impact loading. When high impact loading was applied, cracks propagated through stronger regions in the concrete, thereby augmenting the dynamic compressive strength. Conversely, as shown in Figure 14, cracks propagate along weaker regions, such as the interface transition zone, leading to lower static compressive strength in quasi-static tests. Meanwhile, it was found that the dynamic compressive strength was enhanced with an increasing RSF content, whereas it declined with an increasing CR content. RSFs were demonstrated to play a role in bridging cracks and inhabiting crack propagation, thus enhancing dynamic compressive strength, which was demonstrated in previous studies at both macro and micro levels [4]. However, an increase in CR particles was found to cause the formation of more soft spots inside the concrete due to CR's poor mechanical properties and the weak bonding between CR and concrete, leading to a decreasing trend in dynamic compressive strength [51]. It was demonstrated from a microscopic perspective by the test

results by Ma et al. [52]. The smooth ITZ and the presence of pores within the RuAAC remained noticeable after CR peeling. The widespread existence of these minuscule pores in the aggregate's ITZ contributed to a notable reduction in the dynamic compressive strength of the RuAAC.

Table 7. Results of SHPB test.

Mix ID	Static Compressive Strength/MPa	Pressure /MPa	Dynamic Compressive Strength/MPa	DIF	Toughness /(kJ/m^3)
RSF1-R0	66.3	0.5	109.5	1.65	272.0
		0.6	113.0	1.70	261.5
		0.7	128.0.	1.93	471.5
		0.8	136.0	2.05	426.7
		0.9	146.8	2.21	503.5
RSF2-R0	79.6	0.5	115.4	1.45	271.0
		0.6	122.3	1.54	320.1
		0.7	134.3	1.69	482.3
		0.8	147.8	1.86	605.7
		0.9	156.0	1.96	668.9
RSF3-R0	81.2	0.5	126.2	1.55	301.1
		0.6	137.4	1.69	436.0
		0.7	145.8	1.80	540.2
		0.8	151.0	1.86	633.8
		0.9	165.2	2.03	688.8
RSF2-R5	70.3	0.5	109.5	1.56	272.0
		0.6	118.3	1.68	345.4
		0.7	129.6	1.84	540.9
		0.8	140.0	1.99	538.4
		0.9	148.0	2.11	634.0
RSF2-R20	56.7	0.5	103.6	1.83	268.0
		0.6	109.6	1.93	358.7
		0.7	117.4	2.07	413.9
		0.8	127.7	2.25	536.7
		0.9	139.5	2.46	669.3
RSF2-R35	43.3	0.5	87.7	2.03	248.6
		0.6	90.2	2.08	307.9
		0.7	100.4	2.32	410.1
		0.8	108.3	2.50	467.0
		0.9	121.6	2.81	582.9
RSF2-R50	30.7	0.5	73.0	2.38	180.3
		0.6	82.7	2.69	217.5
		0.7	95.5	3.11	303.7
		0.8	103.4	3.37	360.8
		0.9	114.2	3.72	537.8

Figure 15 shows the influence of different impact pressures on the dynamic increase factor (DIF) of the RuAAC. The DIF is the ratio of the dynamic compressive strength to the quasi-static compressive strength and is used to quantify the stress–strain sensitivity and characterize the extent of strength enhancement in materials under impact loading. An increase in the DIF value typically indicates that a material's strength is enhanced compared to static loading conditions. Specifically, a higher DIF value implies that the material exhibits greater toughness or durability under high-speed loading conditions. From Table 7 and Figure 15, the DIF was found to be greater than 1 and increased with the impact pressure increasing. Figure 15a indicated that the DIF of the RuAAC was between 1.6 and 2.2, with no clear pattern when the RSF content increased. This may be because the inclusion of RSFs can cause a bridging effect and inhibit crack development when subjected

to impact loading, limiting the lateral deformation of the RuAAC. This results in a transition from a one-dimensional stress state to a two-dimensional strain state, leading to an increase in the DIF. Figure 15b shows that the DIF also increased when the CR content increased. For RSF2-R50, the DIF values at impact pressures of 0.5 MPa, 0.6 MPa, 0.7 MPa, 0.8 MPa and 0.9 MPa were 2.37, 2.69, 3.11, 3.37 and 3.73, respectively, corresponding to increases of 63.4%, 74.7%, 84%, 82.2% and 90.3% compared to RSF2-R0. This may be because when cracks pass through CR particles, the crack-arresting mechanism of stress relaxation due to CR particles reduced the crack propagation rate. Additionally, the low elastic modulus of CR particles enhanced the strain capacity of the RuAAC, thereby significantly improving the energy dissipation capacity. It is worth noting that under the same impact pressure, as shown in Figure 15b, the addition of rubber consistently increased the DIF of the RuAAC when the RSF content was 2%. This demonstrated a synergistic effect between the RSFs and CR, enhancing the impact resistance performance of the RuAAC, consistent with the results in Ref. [41]. Overall, the high DIF values, that is, the obvious strain rate sensitivity exhibited by the RuAAC in the SHPB tests, indicated a superior impact performance particularly suitable for architectural structures prone to seismic or explosive impacts.

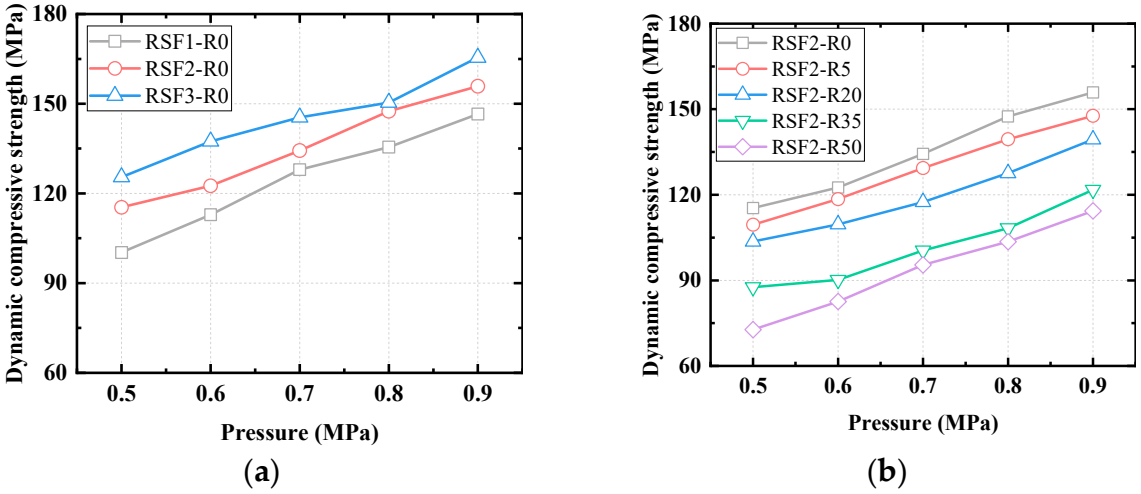

Figure 13. Influence of different levels of impact pressure on dynamic compressive strength: (**a**) RSF content; (**b**) rubber content.

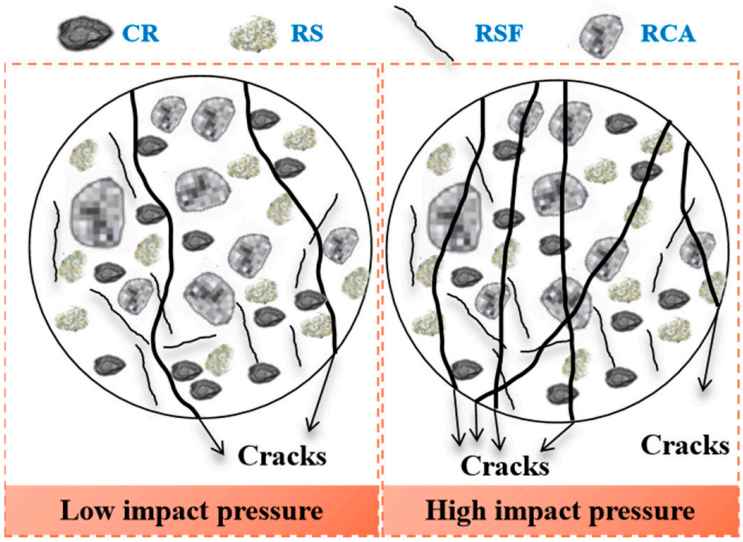

Figure 14. Crack propagation patterns of RuAAC specimens under different impact pressures.

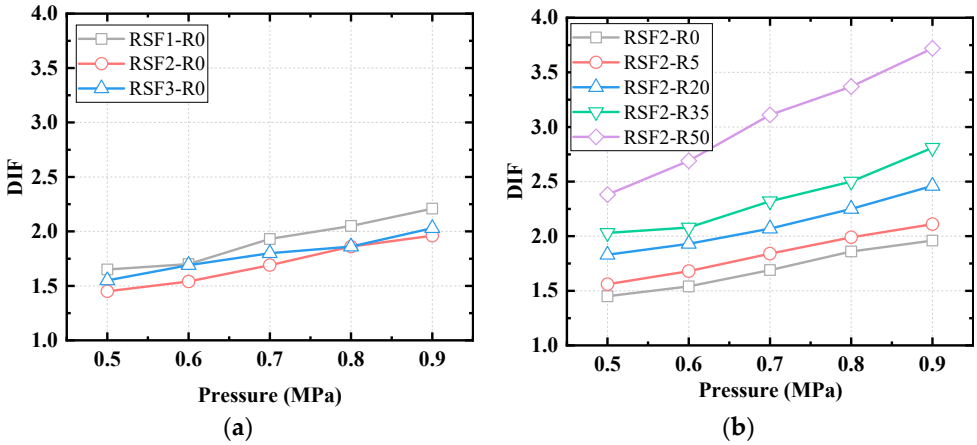

Figure 15. Influence of different levels of impact pressure on DIF: (**a**) RSF content; (**b**) rubber content.

4.2.4. Toughness

Concrete's ability to resist impact loads is determined by its combination of load-carrying and energy-absorbing capacities, referred to as impact toughness [53]. Previous studies have proposed various methods to define impact toughness [36,53–55]. In SHPB tests, impact toughness is commonly calculated based on the pre-peak area of stress–strain curve [56]. While this approach might overlook the contribution of the post-peak portion of the curve to toughness, the unloading of impact forces may occur after the peak point, potentially not accurately reflecting the concrete's true stress–strain state [53]. Therefore, the commonly adopted method in previous studies was to use the integration before the curve's peak point as a measure of impact toughness [56–58]. Specifically in this study, Equation (1) was adopted to calculate the impact toughness of the RuAAC.

$$\omega = \int_0^{\varepsilon_0} \sigma(\varepsilon) d\varepsilon \tag{4}$$

where ε_0 is the peak strain corresponding to the peak stress of the dynamic stress–strain curve.

Figure 16 presents the variation in the impact toughness of the RuAAC at different levels of impact pressure. As seen in Figure 16a, the toughness of the RuAAC increased with an increase in impact pressure, showcasing obvious sensitivity to impact pressure in the RuAAC. Under static loading, with the input of energy, concrete cracks continuously propagated along weaker areas, slowly releasing energy and accumulating damage until ultimate failure. However, under impact loading, the concrete accumulated a significant amount of energy in a short period. Due to the short loading time, internal cracks in the concrete traversed through the aggregates rather than ITZs to rapidly release the energy, thus dissipating a substantial amount of energy and presenting greater toughness [45,51].

Moreover, as the RSF content increased, the toughness of the RuAAC improved continuously. For instance, the toughness of RSF3-R0 was 22.4% and 66.7% higher than RSF2-R0 and RSF-R0 under 0.7 MPa of impact pressure, respectively. This suggests that RSFs significantly enhanced the energy absorption capacity of the RuAAC, attributed to the bridging effect and the failure delay resulting from the RSFs. In Figure 16b, it can be observed that the toughness of the RuAAC slightly decreased with increasing content, and when the CR content reached 50%, the decrease in impact toughness became more pronounced. On one hand, this may be due to the fact that this study only calculated the integral under the dynamic stress–strain curve before the peak stress as impact toughness, neglecting the contribution of CR particles after that. On the other hand, since the value of impact toughness mainly depends on the magnitude of peak stress and its corresponding strain, the decrease in impact toughness with the increasing CR content in this study may also be attributed to the significant strength loss that occurred when a large number of CR particles was introduced, as shown in Table 7. In fact, although a decrease in impact toughness was observed, it was not significant in the case of RSF2-R35. In comparison,

RSF2-R35 showed a significant decrease in dynamic compressive strength compared to RSF2-R0, indicating the contribution of CR particles to the energy absorption capacity of the RuAAC. The high impact toughness of the RuAAC indicated that it was crucial for optimizing its performance in real-world applications, ensuring structural integrity and enhancing safety in impact-prone environments.

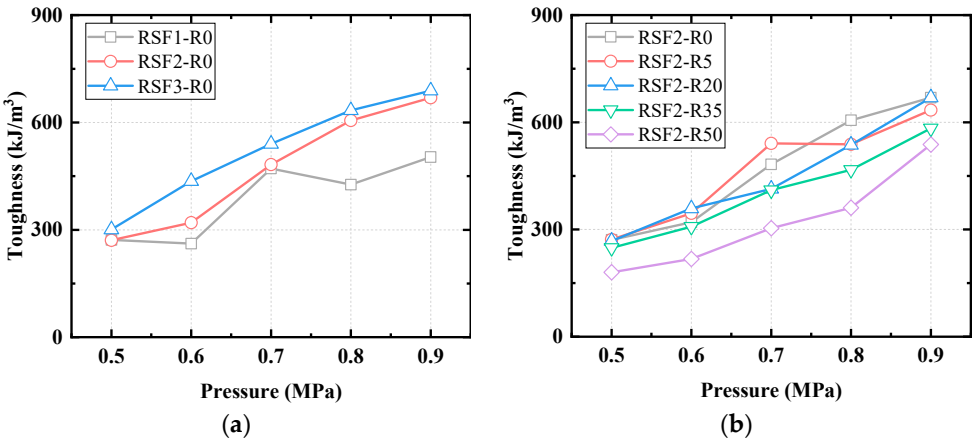

Figure 16. Influence of different levels of pressure on toughness: (**a**) RSF content; (**b**) rubber content.

5. Conclusions

This study proposed an environmentally friendly rubberized alkali-activated concrete incorporating an RCA and RSFs (RuAAC) which is composed mostly of solid waste. Experimental studies on its static and dynamic compressive properties were conducted through axial compression tests and SHPB tests. Variables included different RSF contents (1–3%) and CR contents (0–50%) and five impact pressure levels (0.5 MPa, 0.6 MPa, 0.7 MPa, 0.8 MPa and 0.9 MPa). The main discussion focused on the variation patterns of the RuAAC's failure modes, dynamic stress–strain curves, dynamic compressive strength, DIF and impact toughness. The synergistic effect of the RSFs and CR was discussed. The conclusions of this study can be summarized as follows:

(1) The addition of RSFs enhanced the static mechanical performance of the RuAAC. RSFs can inhibit crack propagation in specimens during loading, thus delaying failure and reducing the brittleness of RuAAC, leading to higher static compressive strength. When CR particles were added, both the strength and elastic modulus of the RuAAC were slightly reduced, attributed to the increased bubbles introduced by the CR, the discontinuity between the matrix and CR particles and the low strength and modulus of elasticity of the CR itself. But RSFs can alleviate the decrease in mechanical properties caused by CR.

(2) With the increases in the RSF and rubber contents, the impact performance of the RuAAC under impact loads improved. Under the same impact pressure level, the integrity of the RuAAC was enhanced.

(3) The RuAAC exhibited significant strain-rate sensitivity which increased with higher rubber and RSF contents, with a more pronounced increase when the rubber content was higher. The synergistic effect of RSFs and CR effectively enhanced the impact resistance of the RuAAC, manifesting in larger DIF values. This evident strain-rate sensitivity and substantial DIF values suggest that the RuAAC has significant potential for applications in building structures susceptible to impact and explosive forces.

(4) At high impact pressures, increasing the RSF and CR contents significantly improved the impact toughness of the RuAAC. The contribution of CR particles to the energy absorption capacity of the RuAAC may have been understated when the integral under the dynamic stress–strain curve before the peak stress was taken as the impact toughness, which neglected potential contributions from CR particles after peak stress.

(5) RuAAC is a concrete material prepared from various solid wastes which demonstrates excellent impact resistance and presents itself as a prospective substitute for conventional concrete. Subsequent research endeavors should focus on two principal domains: firstly, exploring more environmentally friendly and cost-effective retarders and activators; and secondly, devising strategies to enhance the efficacy of constituents such as RSFs, CR and RCAs within the RuAAC matrix to improve its properties.

Author Contributions: Conceptualization, W.C.; methodology, W.C.; formal analysis, L.L.; investigation, Z.C. and D.L.; resources, Y.G.; data curation, L.L. and D.L.; writing—original draft preparation, W.C.; writing—review and editing, Y.G.; visualization, L.L. and Z.C.; funding acquisition, Y.G. All authors have read and agreed to the published version of the manuscript.

Funding: This research was funded by the Maoming Power Supply Bureau, Guangdong Power Grid Co., Ltd. and China Southern Power Grid Co., Ltd., funding number 0309002023030201JJ00031.

Data Availability Statement: The data presented in this study are available on request from the corresponding author. The data are not publicly available due to confidentiality issues.

Conflicts of Interest: Author Weixian Che was employed by the company Grid Planning and Research Center, Guangdong Power Grid Co., Ltd., China Southern Power Grid Co., Ltd. Authors Lei Li and Zhongmin Chen was employed by the company Maoming Power Supply Bureau, Guangdong Power Grid Co., Ltd., China Southern Power Grid Co., Ltd. The remaining authors declare that the research was conducted in the absence of any commercial or financial relationships that could be construed as a potential conflict of interest. The authors declare that this study received funding from Maoming Power Supply Bureau, Guangdong Power Grid Co., Ltd. and China Southern Power Grid Co., Ltd. The funder was not involved in the study design, collection, analysis, interpretation of data, the writing of this article or the decision to submit it for publication.

References

1. Cai, J.; Pan, J.; Han, J.; Lin, Y.; Sheng, Z. Impact behaviours of engineered geopolymer composite exposed to elevated temperatures. *Constr. Build. Mater.* **2021**, *312*, 125421. [CrossRef]
2. Elmesalami, N.; Celik, K. A critical review of engineered geopolymer composite: A low-carbon ultra-high-performance concrete. *Constr. Build. Mater.* **2022**, *346*, 128491. [CrossRef]
3. Ranjbar, N.; Zhang, M. Fiber-reinforced geopolymer composites: A review. *Cem. Concr. Compos.* **2020**, *107*, 103498. [CrossRef]
4. Chen, G.; Zheng, D.-P.; Chen, Y.-W.; Lin, J.-X.; Lao, W.-J.; Guo, Y.-C.; Chen, Z.-B.; Lan, X.-W. Development of high performance geopolymer concrete with waste rubber and recycle steel fiber: A study on compressive behavior, carbon emissions and economical performance. *Constr. Build. Mater.* **2023**, *393*, 131988. [CrossRef]
5. Provis, J.L.; Deventer, J.S.J.V. Alkali Activated Materials: State-of-the-Art Report, RILEM TC 224-AAM. 2014. Available online: https://link.springer.com/book/10.1007/978-94-007-7672-2 (accessed on 17 January 2024).
6. Sakulich, A.R. Reinforced geopolymer composites for enhanced material greenness and durability. *Sustain. Cities Soc.* **2011**, *1*, 195–210. [CrossRef]
7. Lin, J.-X.; Luo, R.-H.; Su, J.-Y.; Guo, Y.-C.; Chen, W.-S. Coarse synthetic fibers (PP and POM) as a replacement to steel fibers in UHPC: Tensile behavior, environmental and economic assessment. *Constr. Build. Mater.* **2024**, *412*, 134654. [CrossRef]
8. Cai, Y.-J.; Xie, Z.-H.; Xiao, S.-H.; Huang, Z.-R.; Lin, J.-X.; Guo, Y.-C.; Zhuo, K.-X.; Huang, P.-y. An investigation of fatigue behavior and residual strength model of steel-GFRP composite bar. *Compos. Struct.* **2024**, *327*, 117685. [CrossRef]
9. Lin, J.-X.; Huang, P.-Y.; Guo, Y.-C.; Guo, X.-Y.; Zeng, J.-J.; Zhao, C.; Chen, Z.-B. Fatigue behavior of RC beams strengthened with CFRP laminate under hot-wet environments and vehicle random loads coupling. *Int. J. Fatigue* **2020**, *131*, 105329. [CrossRef]
10. Chen, Z.; Huang, L.; Huang, P.; Xie, J. Axial-Impact Resistance of CFRP-Confined Ultrahigh-Performance Concrete. *J. Compos. Constr.* **2022**, *26*, 04022059. [CrossRef]
11. Dai, X.; Aydin, S.; Yardimci, M.Y.; De Schutter, G. Rheology and structural build-up of sodium silicate- and sodium hydroxide-activated GGBFS mixtures. *Cem. Concr. Compos.* **2022**, *131*, 104570. [CrossRef]
12. Kumar, S.; Sekhar Das, C.; Lao, J.; Alrefaei, Y.; Dai, J.-G. Effect of sand content on bond performance of engineered geopolymer composites (EGC) repair material. *Constr. Build. Mater.* **2022**, *328*, 127080. [CrossRef]
13. Sun, B.; Sun, Y.; Ye, G.; De Schutter, G. A mix design methodology of slag and fly ash-based alkali-activated paste. *Cem. Concr. Compos.* **2022**, *126*, 104368. [CrossRef]
14. Ahmed, H.; Tiznobaik, M.; Huda, S.B.; Islam, M.S.; Alam, M.S. Recycled aggregate concrete from large-scale production to sustainable field application. *Constr. Build. Mater.* **2020**, *262*, 119979. [CrossRef]
15. Ahmed, W.; Lim, C.W. Production of sustainable and structural fiber reinforced recycled aggregate concrete with improved fracture properties: A review. *J. Clean. Prod.* **2021**, *279*, 123832. [CrossRef]

16. Alsaif, A.S.; Abdulrahman, S.; Albidah, A. Compressive and flexural characteristics of geopolymer rubberized concrete reinforced with recycled tires steel fibers. *Mater. Today Proc.* **2022**, *65*, 1230–1236. [CrossRef]
17. Zhuo, K.-X.; Liu, G.-T.; Lan, X.-W.; Zheng, D.-P.; Wu, S.-Q.; Wu, P.-Z.; Guo, Y.-C.; Lin, J.-X. Fracture Behavior of Steel Slag Powder-Cement-Based Concrete with Different Steel-Slag-Powder Replacement Ratios. *Materials* **2022**, *15*, 2243. [CrossRef]
18. Fang, G.; Zhang, M. Multiscale micromechanical analysis of alkali-activated fly ash-slag paste. *Cem. Concr. Res.* **2020**, *135*, 106141. [CrossRef]
19. Fang, G.; Ho, W.K.; Tu, W.; Zhang, M. Workability and mechanical properties of alkali-activated fly ash-slag concrete cured at ambient temperature. *Constr. Build. Mater.* **2018**, *172*, 476–487. [CrossRef]
20. Sun, Z.; Vollpracht, A. Isothermal calorimetry and in-situ XRD study of the NaOH activated fly ash, metakaolin and slag. *Cem. Concr. Res.* **2018**, *103*, 110–122. [CrossRef]
21. Ismail, I.; Bernal, S.A.; Provis, J.L.; San Nicolas, R.; Hamdan, S.; van Deventer, J.S.J. Modification of phase evolution in alkali-activated blast furnace slag by the incorporation of fly ash. *Cem. Concr. Compos.* **2014**, *45*, 125–135. [CrossRef]
22. Krishna Rao, A.; Kumar, D.R. Effect of various alkaline binder ratio on geopolymer concrete under ambient curing condition. *Mater. Today Proc.* **2020**, *27*, 1768–1773. [CrossRef]
23. Lian, C.; Wang, Y.; Liu, S.; Hao, H.; Hao, Y. Experimental study on dynamic mechanical properties of fly ash and slag based alkali-activated concrete. *Constr. Build. Mater.* **2023**, *364*, 129912. [CrossRef]
24. Elzeadani, M.; Bompa, D.V.; Elghazouli, A.Y. Preparation and properties of rubberised geopolymer concrete: A review. *Constr. Build. Mater.* **2021**, *313*, 125504. [CrossRef]
25. Part, W.K.; Ramli, M.; Cheah, C.B. An overview on the influence of various factors on the properties of geopolymer concrete derived from industrial by-products. *Constr. Build. Mater.* **2015**, *77*, 370–395. [CrossRef]
26. Singh, B.; Ishwarya, G.; Gupta, M.; Bhattacharyya, S.K. Geopolymer concrete: A review of some recent developments. *Constr. Build. Mater.* **2015**, *85*, 78–90. [CrossRef]
27. Aly, A.M.; El-Feky, M.S.; Kohail, M.; Nasr, E.-S.A.R. Performance of geopolymer concrete containing recycled rubber. *Constr. Build. Mater.* **2019**, *207*, 136–144. [CrossRef]
28. Neupane, R.P.; Imjai, T.; Makul, N.; Garcia, R.; Kim, B.; Chaudhary, S. Use of recycled aggregate concrete in structural members: A review focused on Southeast Asia. *J. Asian Archit. Build. Eng.* **2023**, 1–24. [CrossRef]
29. Imjai, T.; Kefyalew, F.; Aosai, P.; Garcia, R.; Kim, B.; Abdalla, H.M.; Raman, S.N. A new equation to predict the shear strength of recycled aggregate concrete Z push-off specimens. *Cem. Concr. Res.* **2023**, *169*, 107181. [CrossRef]
30. Imjai, T.; Garcia, R.; Kim, B.; Hansapinyo, C.; Sukontasukkul, P. Serviceability behaviour of FRP-reinforced slatted slabs made of high-content recycled aggregate concrete. *Structures* **2023**, *51*, 1071–1082. [CrossRef]
31. Kefyalew, F.; Imjai, T.; Garcia, R.; Kim, B. Structural and Service Performance of Composite Slabs with High Recycled Aggregate Concrete Contents. *Eng. Sci.* **2024**, *27*, 1021. [CrossRef]
32. Luhar, S.; Chaudhary, S.; Luhar, I. Thermal resistance of fly ash based rubberized geopolymer concrete. *J. Build. Eng.* **2018**, *19*, 420–428. [CrossRef]
33. Long, W.-J.; Li, H.-D.; Wei, J.-J.; Xing, F.; Han, N. Sustainable use of recycled crumb rubbers in eco-friendly alkali activated slag mortar: Dynamic mechanical properties. *J. Clean. Prod.* **2018**, *204*, 1004–1015. [CrossRef]
34. Ismail Mohamed, K.; Sherir Mohamed, A.A.; Siad, H.; Hassan Assem, A.A.; Lachemi, M. Properties of Self-Consolidating Engineered Cementitious Composite Modified with Rubber. *J. Mater. Civ. Eng.* **2018**, *30*, 04018031. [CrossRef]
35. Li, N.; Long, G.; Ma, C.; Fu, Q.; Zeng, X.; Ma, K.; Xie, Y.; Luo, B. Properties of self-compacting concrete (SCC) with recycled tire rubber aggregate: A comprehensive study. *J. Clean. Prod.* **2019**, *236*, 117707. [CrossRef]
36. Khan, M.Z.N.; Hao, Y.; Hao, H.; Shaikh, F.U.A. Experimental evaluation of quasi-static and dynamic compressive properties of ambient-cured high-strength plain and fiber reinforced geopolymer composites. *Constr. Build. Mater.* **2018**, *166*, 482–499. [CrossRef]
37. Khan, M.Z.N.; Hao, Y.; Hao, H.; Shaikh, F.U.A. Mechanical properties of ambient cured high strength hybrid steel and synthetic fibers reinforced geopolymer composites. *Cem. Concr. Compos.* **2018**, *85*, 133–152. [CrossRef]
38. Zhong, H.; Poon, E.W.; Chen, K.; Zhang, M. Engineering properties of crumb rubber alkali-activated mortar reinforced with recycled steel fibres. *J. Clean. Prod.* **2019**, *238*, 117950. [CrossRef]
39. Zhuo, K.-X.; Cai, Y.-J.; Lai, H.-M.; Chen, Z.-B.; Guo, Y.-C.; Chen, G.; Xiao, S.-H.; Lan, X.-W. Axial compressive behavior of environmentally friendly high-strength concrete: Effects of recycled tire steel fiber and rubber powder. *J. Build. Eng.* **2023**, *76*, 107092. [CrossRef]
40. Peng, G.F.; Niu, X.J.; Long, Q.Q. Experimental Study of Strengthening and Toughening for Recycled Steel Fiber Reinforced Ultra-High Performance Concrete. *Key Eng. Mater.* **2015**, *629–630*, 104–111. [CrossRef]
41. Liu, F.; Chen, G.; Li, L.; Guo, Y. Study of impact performance of rubber reinforced concrete. *Constr. Build. Mater.* **2012**, *36*, 604–616. [CrossRef]
42. *GB/T 14685*; Pebble and Crushed Stone for Construction. China National Standardization Administration: Beijing, China, 2022. Available online: https://openstd.samr.gov.cn/bzgk/gb/newGbInfo?hcno=26E33B40996B9CB1DED15E514B34E7F8 (accessed on 17 January 2024).
43. Su, J.-Y.; Chen, G.; Pan, H.-S.; Lin, J.-X.; Zhang, J.; Zhuo, K.-X.; Chen, Z.-B.; Guo, Y.-C. Rubber modified high strength-high ductility concrete: Effect of rubber replacement ratio and fiber length. *Constr. Build. Mater.* **2023**, *404*, 133243. [CrossRef]

44. *ASTM C469/C469M-22*; Standard Test Method for Static Modulus of Elasticity and Poisson's Ratio of Concrete in Compression. ASTM International: West Conshohocken, PA, USA, 2022. Available online: www.astm.org (accessed on 28 June 2022).
45. Lin, J.-X.; Su, J.-Y.; Pan, H.-S.; Peng, Y.-Q.; Guo, Y.-C.; Chen, W.-S.; Sun, X.-L.; Yuan, B.-X.; Liu, G.-T.; Lan, X.-W. Dynamic compression behavior of ultra-high performance concrete with hybrid polyoxymethylene fiber and steel fiber. *J. Mater. Res. Technol.* **2022**, *20*, 4473–4486. [CrossRef]
46. Guo, Y.-C.; Xiao, S.-H.; Zeng, J.-J.; Zheng, Y.; Li, X.; Liu, F. Fiber reinforced polymer-confined concrete under high strain rate compression: Behavior and a unified dynamic strength model. *Constr. Build. Mater.* **2020**, *260*, 120460. [CrossRef]
47. Feng, W.; Liu, F.; Yang, F.; Jing, L.; Li, L.; Li, H.; Chen, L. Compressive behaviour and fragment size distribution model for failure mode prediction of rubber concrete under impact loads. *Constr. Build. Mater.* **2021**, *273*, 121767. [CrossRef]
48. Pan, H.; Xie, Z.; Chen, G.; Su, J.; Zhuo, K.; Chen, Z.; Lin, J.; Feng, C.; Guo, Y. Dynamic compressive behavior of high-strength engineered geopolymer composites. *J. Build. Eng.* **2023**, *80*, 108036. [CrossRef]
49. Elzeadani, M.; Bompa, D.V.; Elghazouli, A.Y. Compressive and splitting tensile impact properties of rubberised one-part alkali-activated concrete. *J. Build. Eng.* **2023**, *71*, 106596. [CrossRef]
50. Dehdezi, P.K.; Erdem, S.; Blankson, M.A. Physico-mechanical, microstructural and dynamic properties of newly developed artificial fly ash based lightweight aggregate—Rubber concrete composite. *Compos. Part B Eng.* **2015**, *79*, 451–455. [CrossRef]
51. Zhuang, J.; Xu, R.; Pan, C.; Li, H. Dynamic stress–strain relationship of steel fiber-reinforced rubber self-compacting concrete. *Constr. Build. Mater.* **2022**, *344*, 128197. [CrossRef]
52. Ma, Q.; Shi, Y.; Xu, Z.; Ma, D.; Huang, K. Research on a multivariate non-linear regression model of dynamic mechanical properties for the alkali-activated slag mortar with rubber tire crumb. *Case Stud. Constr. Mater.* **2022**, *17*, e01371. [CrossRef]
53. Li, N.; Jin, Z.; Long, G.; Chen, L.; Fu, Q.; Yu, Y.; Zhang, X.; Xiong, C. Impact resistance of steel fiber-reinforced self-compacting concrete (SCC) at high strain rates. *J. Build. Eng.* **2021**, *38*, 102212. [CrossRef]
54. Fu, Q.; Xie, Y.; Long, G.; Niu, D.; Song, H.; Liu, X. Impact characterization and modelling of cement and asphalt mortar based on SHPB experiments. *Int. J. Impact Eng.* **2017**, *106*, 44–52. [CrossRef]
55. Zhang, H.; Liu, Y.; Sun, H.; Wu, S. Transient dynamic behavior of polypropylene fiber reinforced mortar under compressive impact loading. *Constr. Build. Mater.* **2016**, *111*, 30–42. [CrossRef]
56. Bai, Y.-l.; Yan, Z.-W.; Jia, J.-F.; Ozbakkaloglu, T.; Liu, Y. Dynamic compressive behavior of concrete confined with unidirectional natural flax FRP based on SHPB tests. *Compos. Struct.* **2021**, *259*, 113233. [CrossRef]
57. Ren, G.M.; Wu, H.; Fang, Q.; Liu, J.Z. Effects of steel fiber content and type on dynamic compressive mechanical properties of UHPCC. *Constr. Build. Mater.* **2018**, *164*, 29–43. [CrossRef]
58. Wang, S.; Zhang, M.-H.; Quek, S.T. Mechanical behavior of fiber-reinforced high-strength concrete subjected to high strain-rate compressive loading. *Constr. Build. Mater.* **2012**, *31*, 1–11. [CrossRef]